ACS APPLIED POLYMER MATERIALS

pubs.acs.org/acsapm

Article

Stretch-Induced Microstructural Evolution of Electrospun Polycaprolactone Microfibers for Biomedical Applications

Alana Chandler, Ryan M. Schofield, Pierre-Alexis Mouthuy, and Hazel E. Assender*

Cite This: ACS Appl. Polym. Mater. 2025, 7, 8504−8518

Read Online

ACCESS | Metrics & More | Article Recommendations | Supporting Information

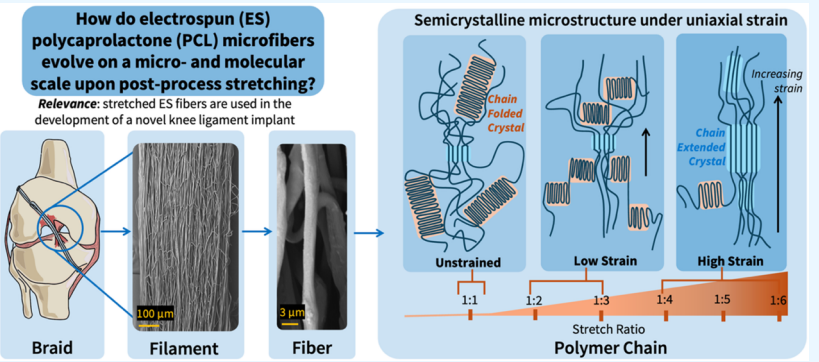

ABSTRACT: The performance and degradation of polymeric medical yarns are strongly dependent on their microstructure, which can evolve significantly during fabrication. This work investigates and models how the microstructure of microfibrous electrospun (ES) filaments changes during the critical postprocessing step of uniaxial stretching. Specifically, we studied filaments designed for use in a knee ligament regeneration implant made from biodegradable, semicrystalline polycaprolactone (PCL). Structural changes were characterized at both the fiber and the molecular scales. Stretching led to fiber alignment, thinning, and coalescence, as revealed by microcomputed tomography (μCT) and scanning electron microscopy (SEM). At the molecular scale, the crystalline microarchitecture transformed profoundly, as shown by differential scanning calorimetry (DSC), one-dimensional (1D) and two-dimensional (2D) X-ray diffraction (XRD), and dynamic mechanical thermal analysis (DMTA). Based on these findings, we propose a conceptual model for stretch-induced microstructural evolution: at lower strains, chain-folded crystals (CFCs) fragment while amorphous chains extend; at higher strains, CFCs unfold and recrystallize with extended chains into more thermodynamically stable chain-extended crystals (CECs) aligned with the stretch axis. This mechanism clarifies how uniaxial strain reorganizes semicrystalline domains in PCL, with important implications for thermomechanical and degradative properties relevant to implant performance. Understanding how microstructure responds to stretching enables the future development of more accurate simulations of complex fibrous materials under physiological conditions and informs the optimization of fabrication and design parameters for next-generation medical yarns.

KEYWORDS: *electrospinning, polycaprolactone, polymer crystals, microfibers, medical yarn, strain-induced crystallization*

1. INTRODUCTION

Implantable polymeric textiles are a promising alternative to biological grafts in promoting the repair of soft tissues such as tendons and ligaments.[1] Bioactive yarns can be designed to provide structural support and guide cell growth for healing tissues by mechanically and morphologically mimicking the hierarchical, anisotropic, and porous structure of the surrounding extracellular matrix (ECM).[2,3] In particular, continuous electrospun (ES) filaments made up of aligned microfibers are of growing interest for such applications.[2] Electrospinning is an electrohydrodynamic process in which a high-voltage electrostatic field is applied between a polymer solution and a conductive collector to produce a nonwoven fibrous mesh.[4] A variety of polymers can be made into biodegradable, biocompatible ES filaments: natural polymers, such as silk fibroin, collagen, and gelatin, and synthetic polymers, such as polycaprolactone (PCL), polydioxanone (PDO), poly(glycolic acid) (PGA), poly(L-lactic acid) (PLLA), as well as copolymers of the aforementioned materials.[5] Research has demonstrated that continuous ES filaments can be transformed into mechanically competent devices comprised of multifilament yarns processed through

Received: March 13, 2025
Revised: June 19, 2025
Accepted: June 23, 2025
Published: July 1, 2025

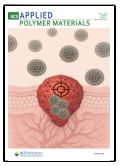

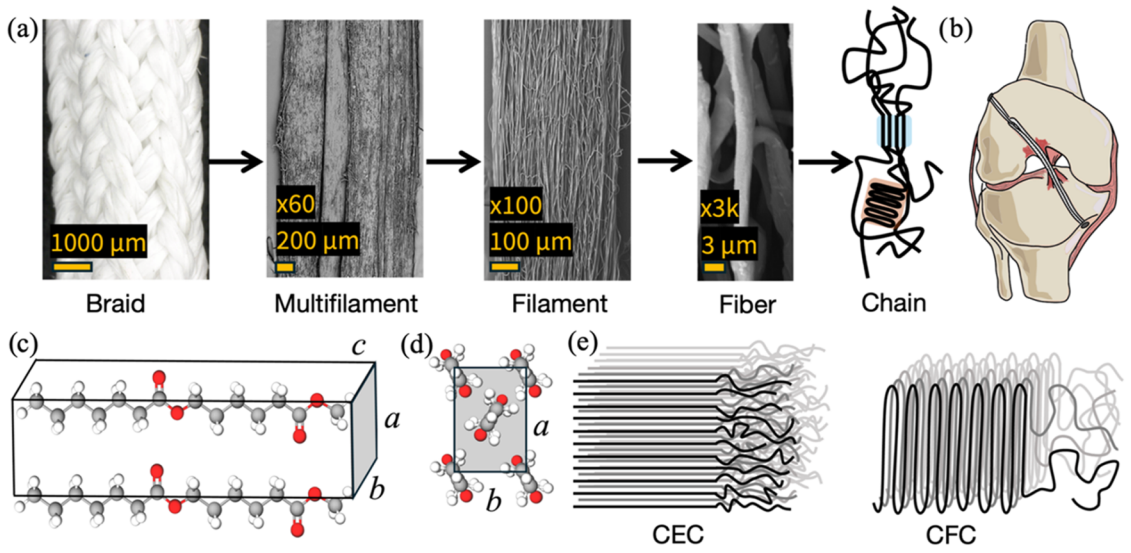

Figure 1. (a) Hierarchical structure of the microfibrous device, progressing from largest to smallest dimension (left to right). Braid image is a macropicture, whereas multifilament, filament, and fiber images are from scanning electron microscopy (SEM), and chain image is a schematic. (b) Schematic of braided implant within the knee. (c) Orthorhombic PCL unit cell (lattice parameters a = 7.496 Å, b = 4.974 Å, c = 17.297 Å) containing a total of two chains in opposite orientation with twists near the ester linkage and a c-axis that coincides with the chain axis,[10,21,22] viewed along b-axis and (d) c-axis. Only chains passing through the frontmost face of the unit cell are depicted for viewing simplicity. (e) Polymer crystal morphologies: chain-extended crystal (CEC) (left) and chain-folded crystal (CFC) (right).

the use of traditional textile technologies such as braiding, weaving, and twisting.[6,7]

Of particular importance, our team has recently developed a braided ES PCL yarn for anterior cruciate ligament (ACL) repair, as shown in Figure 1a,b.[4,8] PCL, a synthetic polyester with an orthorhombic unit cell (Figure 1c,d), is among the most widely used resorbable polymers in tissue engineering due to its low inflammatory response, slow degradation rate, ease of processing, and elasticity (Figure S1).[1,9,10] This implantable braid is designed to eliminate the need for autografts in reconstruction surgeries, which carry the risk of donor site morbidity and an increased likelihood of developing secondary osteoarthritis.[11] Composed primarily of microfibrous filaments, the braid features a hierarchical structure that results in complex structure−property relationships. The macroscopic properties of the braid are not simply the sum of the properties observed at the microstructural levels.[12]

A critical step in manufacturing the ES yarns used in this device is uniaxial stretching of the filaments following electrospinning. The purpose of this stretching is 2-fold: (i) mechanically, it contributes to making the filaments sufficiently stiff for its application and limits further plastic deformation after implantation; and (ii) structurally, it aligns the microfibers to mimic ligaments' ECM architecture. Microscopically, stretching can also affect crystallinity—including crystal orientation, degree of crystallinity (X_c), and supramolecular morphology[10,13−16]—which influence the material's viscoelastic behavior. Notably, although other semicrystalline polymers commonly exhibit unit cell transitions following stretching, no such polymorphisms have been observed in PCL.[17] Although previous studies have examined the microstructural evolution of PCL fibers during stretching,[10,18−20] a consistent mechanism has not been established due to variations in materials, processing conditions, and experimental techniques. Thus, it is of significant value to comprehensively investigate fiber- and chain-level architectures using multiple experimental methods to aid in better future understanding, prediction, and tailoring of the mechanical and degradative properties of biomedical filaments.

At the chain level, thermodynamic considerations predict that linear polymers, such as PCL, present two maxima of crystal morphological stability: chain-extended crystals (CECs) and chain-folded crystals (CFCs) (Figure 1e).[23,24] Multiple studies have confirmed that PCL crystallizes into both morphologies,[17,25−27] most using small-angle X-ray scattering (SAXS) to determine long period and lamellar thickness. For a polymer with uniform molecular weight, a fully extended CEC morphology represents the lowest free energy state,[28−30] as chain folding incurs additional fold surface energy.[28,31] Thus, in theory, CECs will melt at a higher temperature than CFCs of the same size, when applying Lindenmeyer's simplifying assumptions.[28] While no studies exist that experimentally investigate T_m differences between CFCs and CECs in PCL, other semicrystalline polymers reflect these ideal thermodynamic predictions of morphological stability.[28,29,31−35]

Building on this general understanding of polymer crystallization behavior and thermodynamic stability, we present a PCL-based case study of the crystal microstructure of ES microfibers subjected to varying degrees of stretch following electrospinning. This work assessed the impact of stretching on fiber diameter and alignment, as well as on crystal morphology, volume, orientation, and overall X_c. The microfibers were analyzed using microcomputed tomography (μCT), scanning electron microscopy (SEM), differential scanning calorimetry (DSC), X-ray diffraction (1D and 2D XRD), and dynamic mechanical thermal analysis (DMTA)—employing experimental methods that no one study on ES PCL microfibers has yet to do in conjunction. Finally, a theoretical framework was developed to describe the evolution of the material's chain-level microstructure. This microstructural study contributes to understanding how multiscale features influence device behavior, enabling future researchers to build upon phenomenological models—based on macroscale viscoelastic and tensile properties of the braid and

https://doi.org/10.1021/acsapm.5c00907
ACS Appl. Polym. Mater. 2025, 7, 8504−8518

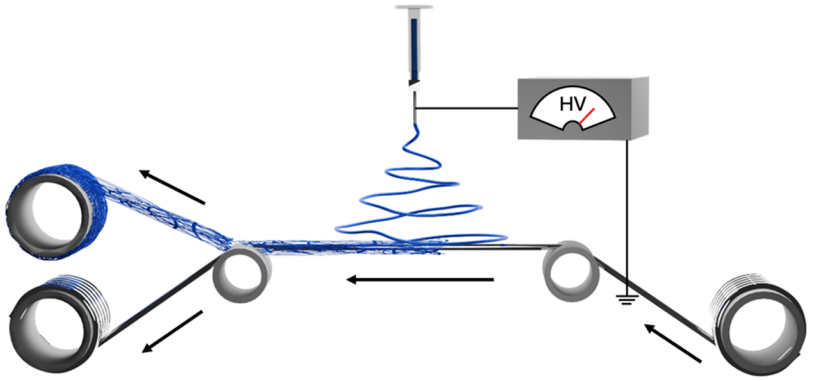

Figure 2. Schematic of the unique electrospinning process used to fabricate our filaments, implementing a moving wire collector.

filaments—for more accurate simulations of complex fibrous structures.[4] Establishing a relationship between microstructural evolution and postprocessing of ES filaments will also guide the design of durable medical yarns to meet the functional demands of orthopedic implants. Our results not only generally align with trends observed in existing related studies but also provide new insights.

2. EXPERIMENTAL METHODS

2.1. Material Preparation. To prepare the ES filaments, poly(ε-caprolactone) (PCL) pellets (Ashland Specialties Ireland, Laboratory A, Synergy Centre, Institute of Technology Tallaght, Ireland) were dissolved in 1,1,1,3,3,3-hexafluoroisopropanol (Apollo Scientific Ltd., Cheshire, U.K.) to 9% w/v PCL. The solution was agitated at room temperature (RT) at 21 rpm (Stuart Roller Mixer SRT9D, Staffordshire, U.K.) for 1 week to ensure complete polymer dissolution. To form a continuous filament of randomly deposited microfibers, a unique electrospinning setup using a dynamic wire collector was used (Figure 2). A detailed description of this electrospinning technique developed by Mouthuy et al. is referenced.[36] Unless otherwise noted, for all experiments, PCL with a weight-average molecular weight, Mw = 1 90 000 g mol^{-1} was investigated (as measured by gel permeation chromatography presented in Figure S2). Triplicates of each sample and their standard deviation were measured. Filaments were stored at 0 °C prior to their usage in experiments to limit ambient material changes.

To measure how the stretch ratio affects polymer crystal properties, filaments were stretched manually to varying degrees at RT, unless otherwise noted, after electrospinning. To ensure uniform stretching along the length of the sample, samples were stretched in 1 cm segments. The maximum stretch ratio reached was 1:6.

2.2. Stretch Temperature. To examine whether different thermal conditions for stretching impacted coalescence, filaments were stretched in RT (20 °C) and cold conditions (immersed in 0 °C ice water) to 1:3 and to maximum stretch. Due to a lower maximum achievable extension in cold conditions (1:5), "dual thermal" samples were also prepared: initially stretched to 1:5 in cold conditions, then allowed to thermally equilibrate to RT before being further stretched to a maximum 1:6 at RT.

2.3. Microfiber Morphology. The diameter and alignment of fibers within filaments stretched to various degrees (1:1−1:6) were observed by using SEM (Hitachi TM3000). A multifilament yarn stored at RT for over 5 months was also imaged to observe any longitudinal changes. Prior to SEM imaging, samples were gold-sputtered to mitigate the effects of charging on image contrast. 2D image analysis was carried out using ImageJ. For fiber diameter, "individual" and "wide" measurements were taken; "individual" denotes measurements from only single fibers (including fibers within coalesced fiber bundles), whereas "wide" measurements classify coalesced fibers as a single fiber alongside individual unfused fibers. "Expected" diameters were also calculated based on the theoretical assumption that stretching along the filament axis directly corresponded to fiber narrowing (see the Supporting Information (SI) 5.1.1 for calculation). Anisotropy was quantified using coherency values from the OrientationJ plugin, where a coherency of 0 corresponded with a completely isotropic image, and 1 corresponded with a completely anisotropic image exhibiting only one orientation.[37] Images with 500× and 3000× magnifications were used for coherence and diameter measurements, respectively.

Filaments were also scanned in a Zeiss Xradia 510 μCT at 70 kV with an imaging voxel size of 0.7 μm. 1:1 and 1:6 filaments were placed in a tube mounted vertically in the scanner. 3D visualization was performed on MeshLab, using compressed data. Coherence was measured using the OrientationJ plugin in ImageJ on these reconstructed images from various depths within the filament, including the surface, center, and midpoint between these latter two (i.e., half radius).

2.4. Thermal Analysis. DSC (PerkinElmer Diamond) was used to obtain heat flow profiles and X_c from samples measured across a thermal range of 0−80 °C under a nitrogen atmosphere. A heating rate of 10 °C min^{-1} was used, unless otherwise indicated. Between the two heating cycles, a faster cooling rate of 100 °C min^{-1} was used. DSC curve characterization and integration was performed using OriginPro software. All DSC curves presented in this work were shifted vertically for ease of visual representation.

To determine the DSC-derived X_c, the following equation was used on the first heating cycle:[38]

$$X_c = \frac{\int_0^\infty \left(\frac{dH}{dt}\right) dt}{\Delta H_{100\%}} \times 100\% \quad (1)$$

where H is the melting enthalpy of the sample per unit mass, t is the time, and $\Delta H_{100\%}$ is the enthalpy of a 100% crystalline sample (139.5 J g^{-1}).[22] H was calculated using eq S1.

A variety of DSC experiments were performed, modulating the following variables: sample type/stretch ratio, stretch temperature, sample−pan contact, and heating rate (the latter two of which are detailed in SI 2.1 and Figures S5−S10).

2.5. Crystallinity and Crystal Size Dimensions. The 1D XRD profile was recorded using Cu Kα radiation (λ = 1.5419 Å) operated at 40 kV and 15 mA on the Rigaku MiniFlex XRD in the range of 2θ = 2−30° at a scanning speed of 1.5° min^{-1}. After background signal subtraction and normalization, OriginPro was used to apply a Gaussian fit. The (111) peak of PCL at 22° was fixed with a full width at half-maximum (fwhm) of 0.98, as the amorphous halo in stretched samples obscured the peak, preventing the software from detecting it. This value was selected based on the peak's average fwhm in unstretched samples.

XRD-derived X_c was calculated using the following equation:

$$X_c = \frac{A_c}{A_c + A_a} \quad (2)$$

https://doi.org/10.1021/acsapm.5c00907
ACS Appl. Polym. Mater. 2025, 7, 8504−8518

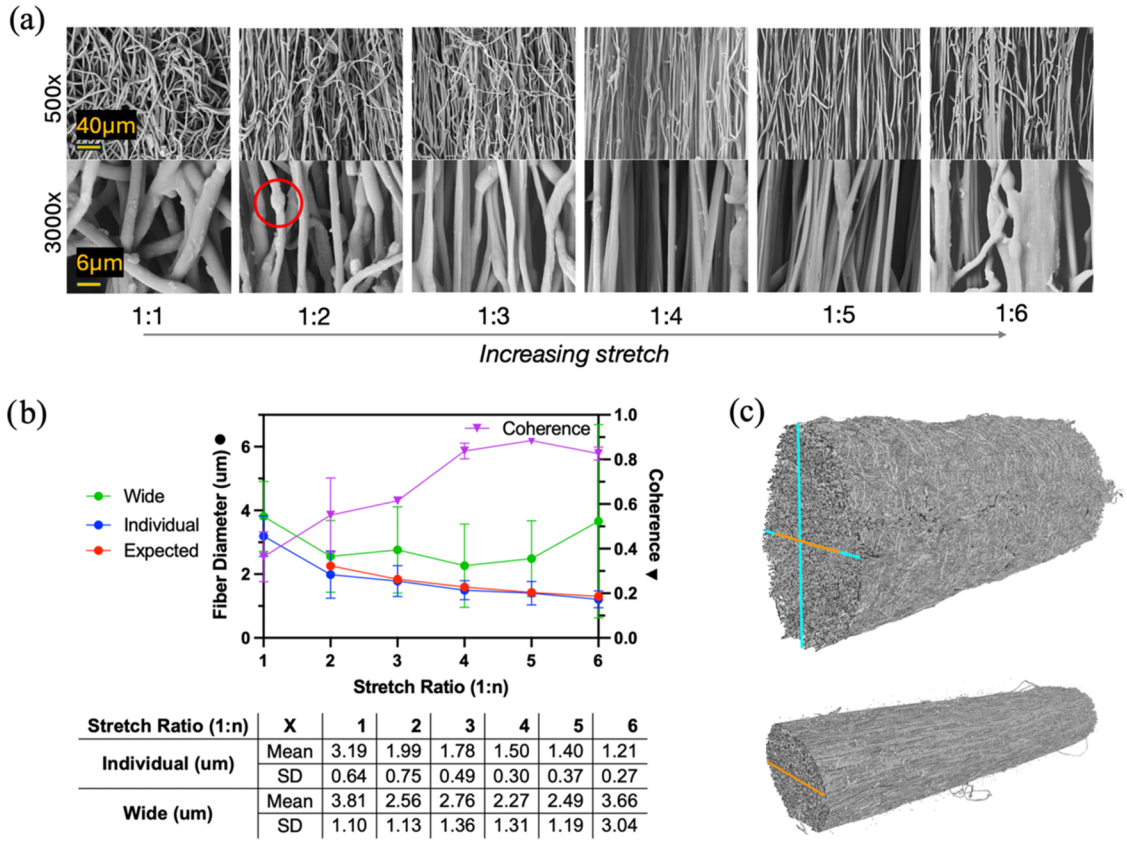

Stretch Ratio (1:n)	X	1	2	3	4	5	6
Individual (um)	Mean	3.19	1.99	1.78	1.50	1.40	1.21
	SD	0.64	0.75	0.49	0.30	0.37	0.27
Wide (um)	Mean	3.81	2.56	2.76	2.27	2.49	3.66
	SD	1.10	1.13	1.36	1.31	1.19	3.04

Figure 3. SEM analysis of fibers: (a) SEM micrographs (top: 500× magnification, bottom: 3000×) of ES PCL fibers at different stretch ratios, from 1:1 to 1:6 (left to right). Fibers exhibit narrowing diameter, coalescence, and bifurcation when stretched. Histogram of diameters displayed in Figure S14. (b) Coherence of filament exterior and mean fiber diameter (green = wide fibers included, blue = individual only, and red = expected) at different degrees of stretch, measured from SEM micrographs. For calculation of the "expected" value, refer to eq S9 in SI 5.1.1. (c) 3D μCT rendering of 1:1 unstretched (top) and 1:6 stretched (bottom) filament. Scaling: orange horizontal = 323 μm, blue horizontal = 470 μm, and blue vertical = 670 μm.

where A_c is the crystalline peak area and A_a is the amorphous halo area.

Crystal size dimension L_{hkl} was calculated for each characteristic peak using the Scherrer equation:

$$\langle L\rangle_{hkl} = \frac{K\lambda}{B\cos\theta} \quad (L < 200\,\text{nm}) \tag{3}$$

where K is the geometric constant (0.94), λ is the X-ray wavelength, B is the fwhm, and θ is the Bragg angle. Average lateral crystal dimension (relative to the crystal c-axis) was calculated by using the (110) and (200) peaks. While smaller crystals cause peak broadening, other potential contributions, such as crystal defects, are detailed in SI 3.1. The lattice parameter was calculated using eq S2, and the tensile force applied to the unit cell was estimated using eqs S3 and S4.

2.6. Crystal Orientation. To determine the degree of crystal alignment in filaments, quadrant azimuthal profiles were obtained via 2D grazing incidence XRD for 1:1 and 1:6 filaments. A Rigaku SmartLab X-ray diffractometer was employed, equipped with a PhotonMax 9 kW rotating anode source using Cu Kα radiation and a HyPix-3000 2D semiconductor detector at a 150 mm sample-to-detector distance. Incident end optics included a 5 mm X-ray spot size height-limiting slit, parallel beam slit, and 1.0° in-plane parallel slit collimator. Out-of-plane (OOP) diffraction was measured with an asymmetric grazing incidence of 0.2° 2θ in 0.04° steps from 0 to 30° 2θ at a rate of 5° 2θ min^{-1}. In-plane (IP) diffraction was captured between −2 and 26° 2θ via a detector offset of 12° 2θ. Background azimuthal intensities near the 2θ of interest were subtracted after correcting for the OOP meridian intensity.[39] Filaments were orientated either parallel (∥) or perpendicular (⊥) to the incident X-ray beam. A schematic of in-plane (IP) and out-of-plane (OOP) orientations relative to sample surface face, as well as azimuthal angle β, is provide in Figure S12.

Herman's orientation factor (f) was used to quantify orientation within a system:

$$f = \frac{3\langle\cos^2\phi\rangle - 1}{2} \tag{4}$$

where $\langle\cos^2\phi\rangle$ = average cosine square of the angle ϕ between an individual specimen's orientation and a reference axis. $f = 0$ when the specimen is isotropic, 1 when the specimen is perfectly aligned to and parallel with the reference axis, and −0.5 when it is aligned perpendicular to the reference axis. The reference direction used was the filament (i.e., stretch) axis, which was also the crystal's c-axis along (00l) when the chains comprising the crystal were aligned to the filament.

2D XRD measured each sample's overall crystal orientation ($f_{overall}$), which was a convolution of the orientation of crystals in an individual fiber ($f_{crystal}$), fibers within a filament (f_{fiber}), and filaments within the XRD sample holder with respect to the intended ∥ or ⊥ placement ($f_{filament}$):[22]

$$f_{overall} = f_{crystal} \times f_{fiber} \times f_{filament} \tag{5}$$

$f_{filament}$ was assigned a value of 1, as the filaments were carefully aligned to be practically parallel to one another. To calculate $f_{overall}$, $\langle\cos^2\phi\rangle_{00l}$ was determined using eqs S5−S8, based on Wilchinsky's method for an orthorhombic unit cell as detailed in SI 4.[40] f_{fiber} was determined to account for fiber misorientation from the filament axis.[22,41] To do so, the angular distribution ϕ of fibers from the dominant direction was measured using the ImageJ plugin on SEM

https://doi.org/10.1021/acsapm.5c00907
ACS Appl. Polym. Mater. 2025, 7, 8504−8518

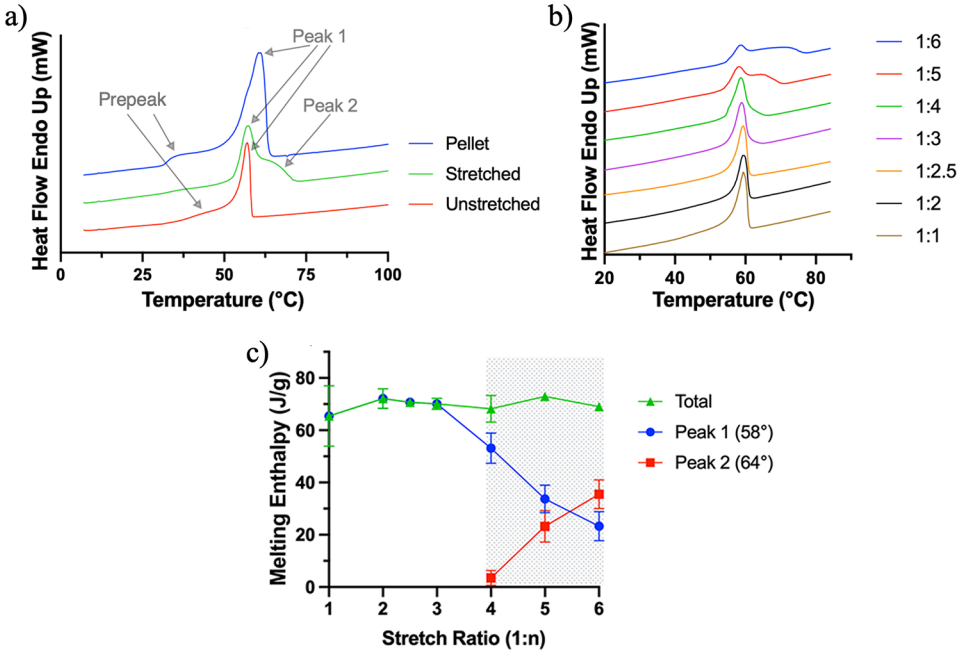

Figure 4. DSC analysis on the effect of stretching on filaments: (a) DSC curves of PCL filaments over first heating cycle with notable features labeled, namely, Prepeak, Peak 1, and Peak 2. (b) DSC curves of filaments stretched to varying degrees (1:1−1:6). (c) Effect of stretching on melting enthalpy on PCL filaments, calculated using eq S1. The shaded region highlights the stretch ratios (1:4 and above) at which curves exhibited secondary endotherm Peak 2.

images at 500× magnification, as shown in Figure S13. An assumption was made that the dominant orientation in the SEM image corresponded to the filament axis.

As described by Wang et al., $f_{crystal}$ is approximated by dividing XRD-derived $f_{overall}$ by SEM-derived f_{fiber}:[22]

$$f_{crystal} = \frac{f_{overall}}{f_{fiber}} \tag{6}$$

2.7. Viscoelasticity. DMTA was used to determine how filament moduli and T_g changed as a function of temperature and stretch. A DMA800 (PerkinElmer) was used, applying a displacement of 0.05 mm in tension at a frequency of 1 Hz. Measurements were performed in a temperature range of −100 to 40 °C at a heating rate of 10 °C min^{-1} in a nitrogen-cooled chamber. Filaments with stretch ratios 1:1, 1:3, and 1:6 were examined. To prevent the samples from slipping out of the DMTA grips, filament ends were cast in Araldite epoxy.

The storage modulus G' (i.e., real; elastic) and loss modulus G'' (i.e., imaginary; viscous) were recorded to calculate $\tan(\delta)$, i.e., the damping factor. $\tan(\delta)$ represents the dissipation of energy in a cyclically deformed material:[42]

$$\tan(\delta) = \frac{G''}{G'} \tag{7}$$

T_g was determined using two points: the temperature at which G'' and $\tan(\delta)$ peaked.[43]

3. RESULTS AND DISCUSSION

3.1. Microfiber Morphology. Figure 3a contains SEM micrographs of microscale segments of filaments stretched to varying degrees, revealing three notable phenomena as a result of stretching. First, stretching reduced the microfiber diameter, although the deformation was not uniformly distributed. Unstretched islands—regions retaining the original filament thickness observed in the 1:1 sample despite stretching of adjacent segments—emerged along the fiber axis due to necking. An example is highlighted by the red circle in Figure 3a. The necked islands, visible from 1:2, disappeared by 1:4 as the material in the islands became consumed by the necking process. Alongside the reduction in fiber diameter was an improvement in fiber alignment (Figure 3b), which plateaued to a peak value of approximately 0.85 by 1:4. Even from a low stretch ratio of 1:2, individual diameters aligned closely with the expected diameter if uniaxial stretching directly corresponded to fiber narrowing (Figure 3b), suggesting that stretching and realignment occur simultaneously. Additional stretching past 1:4 primarily resulted in fiber narrowing, breakage, and subsequent fraying in more random directions, thereby reducing the net alignment (Figure S19). μCT imaging, shown in Figure 3c, was consistent with our SEM results and showed that the coherence of the 1:6 filament (Figure S21) was about 4 times greater than that of 1:1 (Figure S20), as quantified in Table S2. Notably, this also held true for the core of the 1:6 filament, showing that fibers were uniformly aligned across the filament's thickness.

Second, as the stretch ratio increased, some fibers appeared to coalesce together laterally and form a larger fibrous bundle (i.e., "wide" fiber), as observed in Figure 3a. Notably, to our knowledge, no studies outside our own group's have reported stretch-induced coalescence of fibers. Coalescence may result from the local increase in temperature when mechanical work from plastic deformation converts to heat, causing adjacent fibers to merge at local segments. Badami et al. found that an increase in stretch ratio from 1:3 to 1:5 increased the temperature of necked nylon-66 filaments by up to 120 °C, depending on the stretch rate.[44] The increase in temperature causing fiber coalescence can be estimated using energy conservation, as detailed in eqs S10−S13 in SI 5.1.2. The estimated ΔT was 25 °C; thus, at RT a temperature of ∼45 °C may be reached upon stretching. While the main T_m of PCL is 60 °C, our DSC analysis revealed that PCL began to melt at temperatures as low as 40 °C in unstretched filaments (Figure

https://doi.org/10.1021/acsapm.5c00907
ACS Appl. Polym. Mater. 2025, 7, 8504−8518

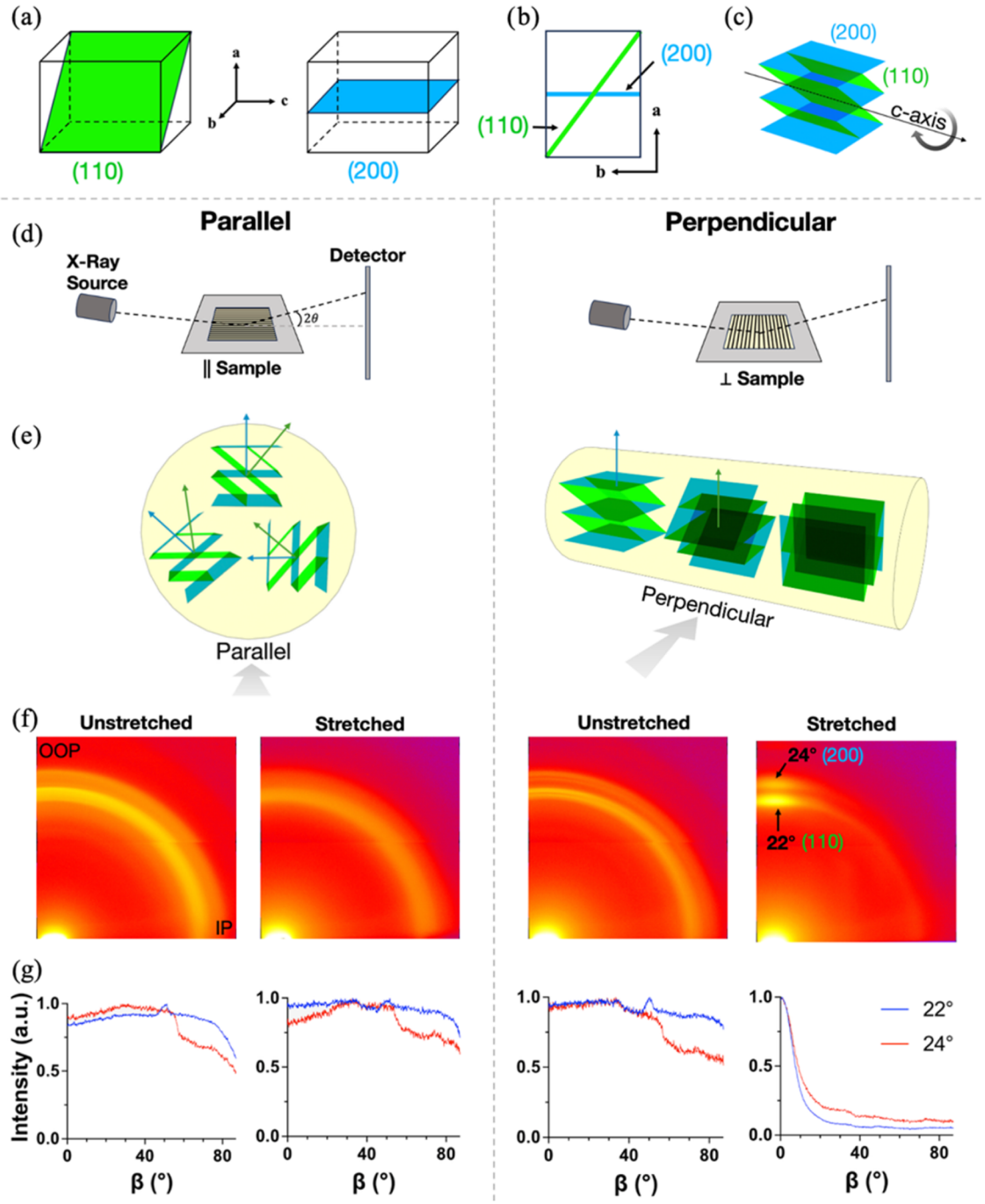

Figure 5. (a) (110) and (200) characteristic crystal planes of PCL, corresponding to distinct diffraction peaks in XRD. Note: unit cell not drawn to proportion. (b) Characteristic planes viewed from the *c*-axis and (c) off-axis, with the *c*-axis as the axis of rotation. (d) Schematic of filament orientation relative to beam in grazing incidence 2D XRD. (e) Simplified X-ray scattering vectors off planes of crystals with their *c*-axis aligned to the fiber axis, with the gray arrow indicating direction of X-ray incidence. (f) 2D XRD profiles showing Debye−Scherrer curves of 1:1 unstretched and 1:6 stretched filaments. Only stretched filaments oriented perpendicular to the beam exhibit discrete diffractions spots. OOP and IP orientations are labeled in the leftmost profile, and characteristic planes are labeled in the rightmost profile. (g) Azimuthal scans presenting diffraction intensity versus azimuthal angle β for 22 and 24° characteristic rings. For parts (d)−(g), figures to the left of the dotted line correspond to filaments oriented parallel to the X-ray beam, and those to the right correspond to filaments oriented perpendicular.

4a). This suggests that coalescence during stretching may be associated with the melting of less stable crystals with a T_m around this temperature.[45] This hypothesis is further supported by comparing the fiber morphology of filaments stretched at different temperatures, specifically when the stretch ratio is sequentially increased by one unit. As presented in the SEM micrographs in Figures 3a and S15 (and plotted in Figure S16), for RT-stretched filaments, no coalescence was observed only for 1:2 filaments, whereas for cold-stretched filaments, their fine microfibrous architecture was maintained up to their maximum possible stretch at this lower temperature, 1:5. From these two positions, the behavior differed upon further stretching at RT. Stretching the 1:2 RT-stretched fiber to 1:3 led to coalescence, whereas RT-stretching of

https://doi.org/10.1021/acsapm.5c00907
ACS Appl. Polym. Mater. 2025, 7, 8504−8518

initially 1:5 cold-stretched filaments to 1:6 (i.e., "dual thermal" filament) presented no coalescence. This discrepancy suggests that filaments that have not been stretched beyond 1:2 possess specific microstructural features that facilitate coalescence, namely, unstable crystals whose lower T_m initiates coalescence.

In addition to strain-initiated coalescence, ambient coalescence (i.e., without strain) was observed in a multifilament yarn stored at RT for 5 months (Figure S17). Here, coalescence likely results from gradual amorphous rearrangement, as RT is above PCL's T_g and below the melting onset temperature of 40 °C. Even without heat dissipation from plastic deformation, unstable crystals may rearrange into more thermodynamically stable structures (i.e., minimization of surface area-to-volume ratio), if the kinetic conditions allow. To prevent coalescence and preserve their fine fibrous architecture, filaments should be stretched and stored at colder temperatures. Other potential mechanisms of ambient crystal transformation include chain scission through humidity-induced hydrolysis, trans-esterification, and Ostwald ripening[46]—all of which could affect X_c and the entanglement environment. Residual solvent may also contribute to ambient coalescence,[47] warranting further investigation through thermogravimetric analysis.

Lastly, stretched filaments exhibited bifurcations—regions where one fiber transitions into two, as depicted in Figure S18. Even filaments at low degrees of stretch exhibit bifurcations. It is not possible to ascertain from these static images whether bifurcations represent fiber splitting or fusing, occurring during spinning or stretching. However, given the lack of coalescence at low degrees of stretch, these bifurcations likely reflect fiber splitting as they align during the initial stages of stretching, whereas bifurcations at high degrees of stretch reflect areas where fibers begin to fuse.

In brief, imaging showed that fibers do not simply narrow uniformly upon stretching but exhibit greater complexities, such as unstretched islands, coalescence, and bifurcations.

3.2. Crystal Orientation. Transitioning our consideration from the fiber- to crystal-scale, diffraction intensity along a Debye−Scherrer ring associated with a particular set of planes in 2D XRD can be measured to compare crystal orientation across samples.[48] The raw detector profiles in Figure 5f show rings corresponding to the (110) planes at $2\theta = 22°$ and (200) at $2\theta = 24°$, matching the literature values.[10,49,50] PCL's characteristic planes are depicted in Figure 5a−c. Only 1:6 filaments oriented ⊥ to the X-ray beam exhibit discrete OOP diffraction spots, whereas other samples/orientations present uniform rings. As depicted in Figure 5d,e, crystals which satisfy diffraction conditions under X-ray illumination perpendicular to the fiber axis are oriented with their (110) and (200) plane normals to the fiber axis, while diffraction is obtained from a range of orientations when the X-ray beam is incident parallel to the fiber axes. Therefore, only in stretched filaments do the (110) and (200) plane normals tend to preferentially lie perpendicular to the fiber axis, with a uniform radial distribution of the associated plane normals perpendicular to the fiber axis. From this observation, we may infer that the polymer backbone is oriented along the stretched fiber axis within crystalline regions.

These azimuthal scans (Figure 5g) allowed for the calculation of $f_{overall}$ (eqs 4−6) shown in Table 1, which was normalized to the orientation distribution f_{fiber} of fibers within the filament (Figure S13) to calculate the crystal alignment $f_{crystal}$ within a fiber. Measuring $f_{crystal}$ for filaments with completely random fiber deposition is not possible; f_{fiber} would be zero, rendering $f_{crystal}$ undefined, even though fibers may possess some degree of crystal alignment. Other potential analytical limitations and sources of artifacts are discussed in SI 4.2. While the accuracy of our deconvolution may be compromised by the low f_{fiber} value from near-random deposition, the slight fiber anisotropy of our 1:1 filaments—perhaps due to the contour of the electric field with the wire collector, or from light tugging of fibers during deposition on the dynamic collector and subsequent removal—nonetheless enabled calculation of $f_{crystal}$.

Table 1. Herman's Orientation Factor f for 1:1 Unstretched and 1:6 Stretched Samples

sample	$f_{overall}$ [XRD]	f_{fiber} [SEM] (n = 3)	$f_{crystal}$
unstretched (1:1)	0.005	0.094 ± 0.045	0.050
stretched (1:6)	0.593	0.941 ± 0.043	0.631

The orientation factor $f_{crystal}$ for 1:6 filaments (0.631) indicated strong alignment, whereas 1:1 filaments (0.050) did not. This means that during straining, crystals, whether pre-existing or newly formed due to tension, tend to align their c-axis along the fiber axis. The rearrangement of crystals along the stretch axis requires interpenetrating amorphous chains to bear the initial tensile load, whose extension may serve as nucleation sites for CECs that are also subsequently aligned with this axis.[51]

3.3. Proposed Mechanism for Strain-Induced Crystal Transformation. Stretching semicrystalline polymers can cause crystal transformation.[37] A large body of literature on polymer crystals grown from the random state (i.e., melt, solution) concludes that nucleation via chain folding drives the formation of CFCs.[52] When subjecting the random state to tensile stress, several studies have observed the formation of CECs in a variety of polymers including PCL, confirmed via electron diffraction, Fourier transform infrared spectroscopy, atomic force microscopy (AFM), SAXS, and DSC.[17,26,34,41,52,53] Although the deformation mechanisms underlying stretching of semicrystalline polymers have been studied extensively both theoretically and experimentally, there remains a lack of consensus as to which mechanism is accurate. For cold-stretching, the most commonly hypothesized mechanisms include CFC-lamellar fragmentation,[35] stack rotation,[54] melt-recrystallization,[42,55] and amorphous extension.[56] Some studies suggest simultaneous occurrence of these phenomena,[45] while others posit sequential incidence as stretching progresses.[55] These models are further detailed in Table S3 and Figure S22.

Based upon our collective experimental findings, a microstructural, chain-based model is proposed to explain the strain-induced crystal transformations observed in ES PCL microfibers (Figure 6). This model is introduced here to contextualize the interpretation of the results presented in the following sections.

To begin, in the unstretched state, filaments are hypothesized to consist predominantly of CFCs, though the presence of some CECs is possible due to polymer jet elongation during electrospinning.[53] At low strains, amorphous chains begin to uncoil and extend in the direction of applied strain, as supported by DMTA, while unstable crystals undergo melt-recrystallization, as observed by DSC. CFCs experience crystal slip and fragment into smaller blocks, as indicated by XRD. At higher stains, it is proposed that fragmented CFCs unfold

https://doi.org/10.1021/acsapm.5c00907
ACS Appl. Polym. Mater. 2025, 7, 8504−8518

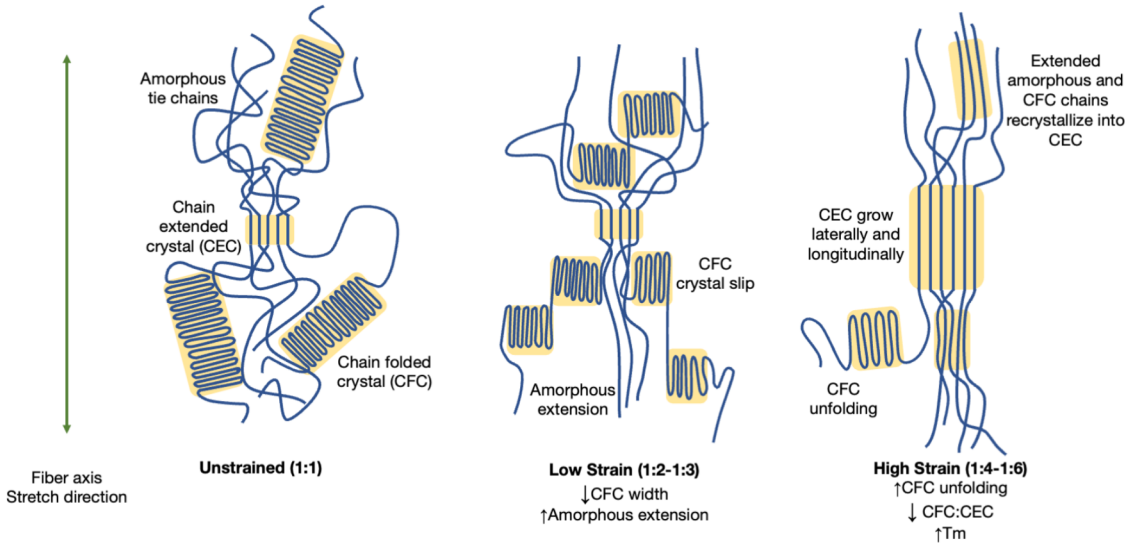

Figure 6. Schematic of chain evolution upon stretching of the ES PCL microfiber. Yellow shading represents crystalline regions. Melt-recrystallization of unstable prepeak crystals not included in the low strain panel.

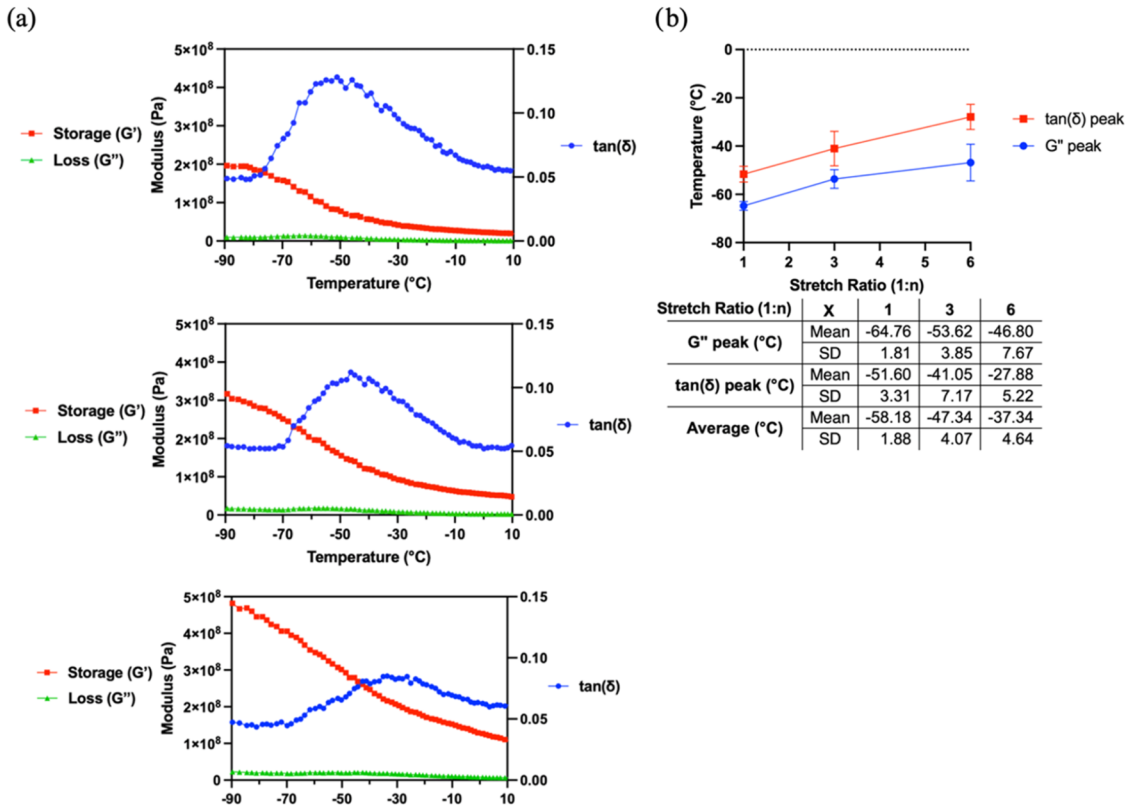

Stretch Ratio (1:n)	X	1	3	6
G" peak (°C)	Mean	-64.76	-53.62	-46.80
	SD	1.81	3.85	7.67
tan(δ) peak (°C)	Mean	-51.60	-41.05	-27.88
	SD	3.31	7.17	5.22
Average (°C)	Mean	-58.18	-47.34	-37.34
	SD	1.88	4.07	4.64

Figure 7. (a) DMTA curves for 1:1, 1:3, and 1:6 filaments (top to bottom). The temperature range for the plots was confined to −90 to 10 °C to exclude measurement discontinuities at lower temperatures and the effects of epoxy softening at higher temperatures, as shown in Figure S23. (b) T_g as a function of stretching, calculated based on the peak temperature of tan(δ) (red) or G'' (blue).

further and that amorphous chains continue to elongate, as supported by DMTA. These extended chains are believed to align and either form new or integrate into existing CECs oriented along the stretch axis. The reduction in chain coiling during strain is expected to favor the formation of multichain fibrillar nuclei—characteristic of CEC crystallization—over single-chain lamellar nuclei typically associated with CFCs.[51] Additionally, as CFCs narrow due to fragmentation, stretching may promote the alignment and extension of terminal amorphous segments of existing CECs, contributing to CEC growth along the stretch axis. Existing CECs may also act as nucleation sites for the lateral incorporation of amorphous chains.

Although the identification of CFCs and CECs is inferred rather than directly proven, this is strongly supported by converging evidence from multiple experimental techniques, namely, DSC, XRD, and DMTA. Together, these data indicate substantial development of a highly oriented and thermody-

https://doi.org/10.1021/acsapm.5c00907
ACS Appl. Polym. Mater. 2025, 7, 8504−8518

namically distinct crystal population under strain. Accordingly, the model posits that in comparison to unstretched filaments dominated by CFCs, stretching increases the fraction of CECs, alongside changes in the crystal size and orientation. While this mechanism is likely a simplification, as it does not account for mixed crystal mesostructures (e.g., shish-kebab formations) or crystal defects, it offers a cohesive framework to interpret the morphological transformations that occur during stretching.

Experimental findings from stretched fibers of other semicrystalline polymers closely parallel our proposed mechanism,[13,24,45] further detailed in Table S4. For example, multiple studies on PCL fibers, using a variety of experimental techniques, have converged on the interpretation that stretching promotes amorphous chain extension,[10,18−20] which act as a precursor to CEC recrystallization.[52] In the following section, we present complementary evidence using DMTA (a technique not employed in the earlier studies) to probe the effects of stretching on the amorphous phase.

3.4. Viscoelasticity. Analyzing the thermally modulated viscoelastic behavior of filaments using DMTA, particularly the glass transition, offers valuable information on the amorphous region. Preceding the discussion on viscoelasticity, it is important to clarify the term "stretched," as all samples are cyclically stretched within the DMTA apparatus, while some filaments are also stretched prior to DMTA analysis. "Stretched" is used to refer to this latter case, as it has been through this text.

Figure 7a displays DMTA curves for filaments that had been stretched to varying degrees. The curve shape and peak location of 1:1 reflect findings in the literature on PCL.[57] Glass transition temperature (T_g), peak tan(δ) (eq 7), and fwhm values acquired from these curves are presented in Tables S5 and S6. Average T_g increased significantly from −58.18 ± 1.88 to −37.34 ± 4.64 °C upon stretching from 1:1 to 1:6 (Figure 7b), whereas the height of the tan(δ) peak decreased from 0.13 ± 0.01 to 0.08 ± 0.01.

The stretch-induced increase in T_g, a key parameter that marks the transition of amorphous chains from rigid to flexible, indicates amorphous chain extension upon stretching. In addition, T_g may rise due to the constraining effects of nearby crystalline regions on the molecular mobility of adjacent amorphous regions. While the DSC results showed that overall X_c was not altered by stretching (see Section 3.7), it is possible that the new strain-induced crystals pose a greater barrier to molecular motion than the original crystals—corresponding to the replacement of CFCs with CECs, rather than their addition. When comparing such a barrier presented by CECs versus CFCs, there is a clear difference in the freedom of their terminal chains, which reside in both the crystalline and amorphous state, as illustrated in Figure 1e. Chains exiting CECs face greater spatial restrictions compared to those exiting CFCs.

In 1:6 filaments, in addition to the upward shift of the tan(δ) T_g peak, this peak was also shallower, indicating lower levels of energy dissipation during the glass transition. While a lower amorphous fraction in the material could explain this phenomenon, because X_c was constant regardless of the stretch ratio (as determined via DSC), this explanation is inapplicable. Instead, the shallower tan(δ) peak may reflect a less coiled amorphous fraction in the stretched filaments. If amorphous chains in 1:6 filaments are more extended, the amplitude of their segmental motion will be reduced due to the increased rigidity of elongated chains. This rigidity decreases the maximum possible energy dissipation during glass transition, thereby lowering peak tan(δ).[58]

While the tan(δ) peak shifted to a higher T with stretching, the peak's fwhm remained constant (Table S6). A wider tan(δ) peak would reflect energetic heterogeneity in amorphous chain mobility,[59] as the varying proximity of these chains to dispersed crystals modulates the energetic barriers to segmental motion within the interconnected network. The consistency of this fwhm is consistent with the observation that X_c remains constant through stretching.

To summarize, both the higher T_g and lower tan(δ) maxima in stretched filaments may be attributed to greater amorphous chain extension. When the DMTA applies a cyclic tensile force on a filament at a temperature around its T_g, either (i) elastic energy is stored in the chains (associated with greater G') or (ii) energy is dissipated during plastic deformation (associated with greater G''), where chains change conformation after overcoming an energy barrier. Elastic storage is greater in stretched filaments because further plastic deformation is more energetically costly for chains that are already extended.[60] For stretched filaments, intrachain bonds bear the tensile load, whereas for unstretched filaments, tension disrupts interchain interactions within coiled amorphous chains. The extended, restricted character of the amorphous regions in 1:6 filaments explains why these filaments present a greater storage modulus G' (i.e., lower maximum tan(δ)) while requiring greater T_g temperatures to enter a rubbery state.

The proposition that amorphous chains are more extended and contain greater elastic potential energy in 1:6 filaments compared to 1:1 is also supported by hot plate experiments. As shown in Figure S24, 1:6 filaments contracted upon heating, while 1:1 filaments did not. On a microstructural level, as T_m is approached during heating, extended chains—in both the amorphous and crystalline domains (i.e., CEC)—gain mobility and take on higher entropy, coiled conformations, thereby shrinking the overall sample. The amorphous chains in 1:1 filaments presumably possessed more relaxed conformations and subsequently did not experience a thermodynamic drive to coil further upon heating.

Stretching of filaments to high stretch ratios results in structures with chains trapped in an extended conformation. This conclusion is supported by DMTA and hot plate experiments, which show that stretched filaments exhibit a higher glass transition temperature, lower maximum energy dissipation during transition, and chain contraction upon heating.

3.5. Secondary Endotherms. The shapes of DSC curves were compared across samples to understand how polymer crystals evolve through processing, from the as-received pellet to filament stretched to varying degrees. These samples' DSC curves are depicted in Figure 4a,b (Figure S3). All filaments exhibited a primary endotherm (Peak 1) with a peak temperature around 60 °C, representing the original crystal population. Three prominent trends emerged from stretching: (i) the lower temperature premelting peak, or "prepeak," disappeared (most evident in the pellet and at low degrees of stretch), (ii) the height of Peak 1 (~60 °C) shortened, and (iii) a secondary higher temperature endotherm "Peak 2" (~70 °C) grew, reaching its greatest size (in height and rightwards width) at 1:6, the maximum stretch ratio before fracture. This growth in Peak 2 width is plotted as fwhm in Figure S4.

DSC peaks with disparate melting temperatures are said to represent two separate crystal morphologies with distinct

https://doi.org/10.1021/acsapm.5c00907
ACS Appl. Polym. Mater. 2025, 7, 8504−8518

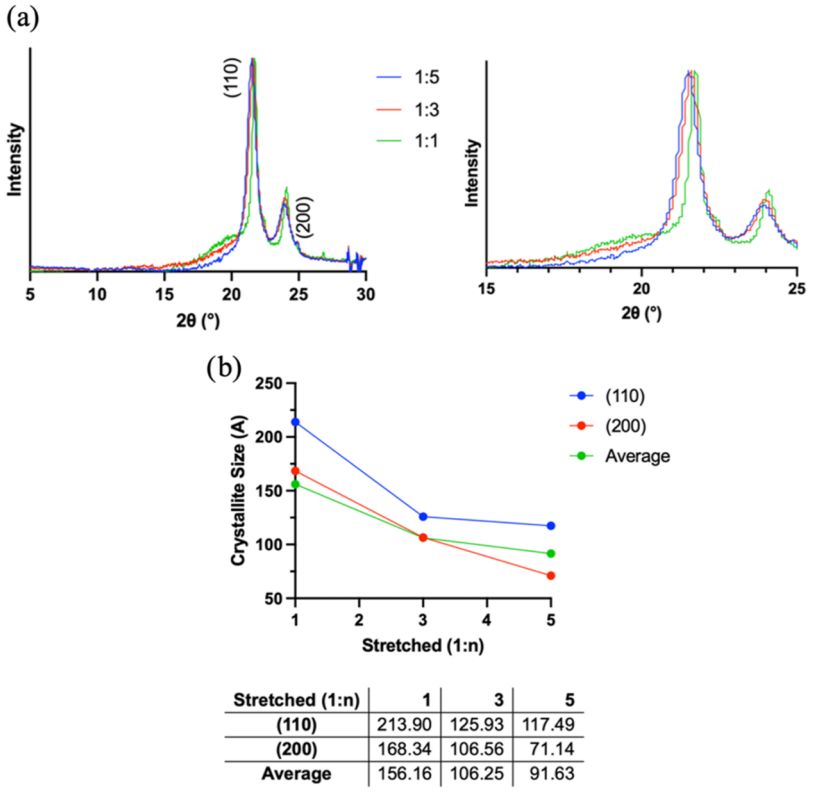

Stretched (1:n)	1	3	5
(110)	213.90	125.93	117.49
(200)	168.34	106.56	71.14
Average	156.16	106.25	91.63

Figure 8. (a) Normalized 1D XRD profile of PCL filaments stretched to various degrees (1:1, 1:3, and 1:5). The right plot presents a magnified view of the left plot, highlighting the peak shifts toward lower angles observed in stretched filaments. (b) Crystal width dimensions (in Å) for characteristic planes as a function of filament stretching. Average includes (111).

thermodynamic stabilities, with the lower endotherm associated with a less stable crystal phase.[61] At the same time, modest reorganization of unstable crystals is possible when slow DSC heating rates are used, whereupon the kinetic barrier to rearrangements is lowered. This represents thermally induced melt-recrystallization, a kinetically controlled process in which imperfect crystals melt and reorganize into more stable forms as chain mobility increases.[62] While similar in overall result, strain-induced melt-recrystallization differs in that it is driven by applied stress, which promotes the formation of more aligned, stable crystals.[54]

Our experiments modulating heating rate and pan contact confirmed that the prepeak and secondary endotherm reflect intrinsic microstructural features of the material rather than measurement artifacts, such as changes in sample−pan contact during DSC heating, as detailed in SI 2.1. The prepeak was absent at slow heating rates (Figure S7), which can be explained by thermally induced melt-recrystallization. Under slow heating, the prepeak melting endotherm is effectively masked by the nearly overlapping exothermic recrystallization. In contrast, Peaks 1 and 2 persisted across the range of DSC heating rates (Figure S8), indicating greater thermal stability. The prepeak thus corresponds to the melting of less stable crystals. Furthermore, its disappearance in stretched filaments (Figure 4a) suggests that strain-induced melt-recrystallization also occurs in response to mechanical deformation.

Notably, modulating heating rate had a greater effect on Peak 2's height compared to Peak 1 in Figure S8, indicating that the activation energy to initiate melting is lower for Peak 2 crystals. This difference in melting kinetics provides further evidence that each peak represents distinct crystal populations. We prospectively assign Peak 2 to CECs because, in addition to Peak 2's greater T_m, studies report that CECs do not undergo melt-recrystallization.[30,63]

Thus, it can be said that stretching induced significant crystal transformations in the fibers, evidenced by the emergence of a higher temperature secondary endotherm Peak 2 after stretching to 1:4. Stretching further, the quantity of Peak 2 crystals increased as that of Peak 1 diminished, as plotted in Figure 4c. The quantity of each crystal subpopulation directly correlates with the peak's area, due to the fact that PCL has only one unit cell polymorph.[17] Section 3.6 further explores the mechanisms of transition in crystal demographics upon stretch.

A recently published study within our research group by Ferreira et al. corroborated our DSC results, revealing the development of a secondary endotherm upon stretching.[4] In their study, the doublet emerged at a higher stretch ratio of 1:9, likely due to experimental differences, including the use of lower Mw (~25 kDa) samples and filament stretching using bollard grips with a constant strain rate. In contrast, the only other DSC study identified on ES PCL, conducted by Selli et al., did not observe a secondary endotherm when stretched to 1:6.[10] This absence may be attributed to the substantially larger diameter of their melt-spun fibers as a result of manufacturing processes that diverged from our electrospinning. A narrower diameter is generally linked to a higher degree of chain extension generated during the spinning process,[64] meaning our narrower fibers may possess more CEC nucleation sites than those of Selli. Of note, studies on ES fibers made from other polymers exhibited higher temperature

https://doi.org/10.1021/acsapm.5c00907
ACS Appl. Polym. Mater. 2025, 7, 8504−8518

secondary endotherms following stretching,[13,14,33,65] which is in agreement with our results.

Analyzing how the secondary endotherm evolves with the stretch temperature also elucidates the mechanism of crystal deformation and resultant morphologies. Tensile plastic deformation can occur through a combination of amorphous extension and crystalline transformation. As shown in Figure S9, it is notable that Peak 2 was much smaller for the 1:5 cold-stretched filament than that of the 1:5 RT-stretched filament. If Peak 2 is associated with strain-induced crystals, the smaller Peak 2 in cold-stretched samples means that less crystal transformation took place, which is expected because crystals are more stable at lower temperatures.

In summary, DSC revealed that stretching decreased the crystal population associated with the prepeak and Peak 1, while the population of Peak 2 increased. Peaks 1 and 2 represent distinct crystal populations with unique morphologies, as evidenced by their differing kinetic barriers to melting and thermodynamic stabilities, the latter of which is reflected in Peak 2's higher T_m. It is important to note that, in addition to the morphology, crystal stability is also influenced by the volume.

3.6. Crystal Volume and Dimensions. DSC and XRD provide insights into how crystal size evolves with stretching. DSC relates crystal volume to thermodynamic stability via T_m, while XRD links size to diffraction peak width.

DSC can be used to compare stretch-induced changes in volume within a specific crystal subpopulation. According to the Gibbs−Thomson effect, smaller crystals have greater surface free energy per unit volume, rendering them less stable and resulting in a lower T_m.[29,30] Stretching increased the breadth of Peak 2 toward higher temperatures (Figure 4b), indicating that crystals within this new population grew larger. While the thermal range that an endotherm spans for a specific crystal population (i.e., Peak 1 or Peak 2) can be used to compare how that subpopulation's volume distribution differs across samples, it is not possible to conclude that Peak 2 crystals are larger than those of Peak 1 just because Peak 2 crystals melt at a higher T_m. This is because the thermal stability is governed by both crystal volume and morphology.

XRD measured changes in the crystal dimensions (eq 3) after stretching. Figure 8a presents the 1D XRD profiles for 1:1, 1:3, and 1:5 filaments. Characteristic (110), (111), and (200) peaks were located at 21.5, 22, and 23.8°, respectively. Notably, at greater degrees of stretch, peaks were broader and shifted slightly toward lower Bragg angles. Scherrer calculations based on peak breadth showed that the average lateral crystal dimensions, perpendicular to the crystal *c*-axis, decreased upon stretching (Figure 8b)—from 191.12 Å in unstretched filaments to 94.32 Å in 1:5 filaments. This trend is reflected in other studies of stretched PCL fibers, as detailed in Table S1. Stretching was also found to increase lattice parameters *a* and *b* (Figure S11). To clarify terminology for the present discussion, width (i.e., wide, narrow) refers to the lateral dimensions of a crystal perpendicular to the molecular *c*-axis, while length refers to that crystal's longitudinal dimension parallel to the *c*-axis.

Pairing these XRD observations with the DSC finding that a morphologically distinct, more stable crystal population formed via stretching, it is possible to conclude that stretching reduces the width of the original crystals or induces the formation of new crystals that are narrower than the original (Figure S25). Because Scherrer calculations provide only an average width across all crystals in the sample, it is challenging to pinpoint which specific crystal population(s) contribute to the overall narrowing upon stretching. The distinct ways in which CFCs and CECs respond to strain along their *c*-axis are theorized in SI 7.1.

DSC showed that the fraction of Peak 1 crystals remained constant up to 1:4 (Figure 4c), while the average crystal width decreased over this interval, as measured by XRD (Figure 8b). Given these observations, the dominant mode of narrowing at low strains is likely fragmentation of CFCs rather than unfolding since unfolding would reduce the fraction of Peak 1 crystals. Straining beyond 1:4, the fraction of Peak 1 crystals decreased, while that of Peak 2 increased. This decrease in the original crystal fraction likely resulted from strain-induced melting via lamellar unfolding. This unfolding, along with amorphous chain elongation evidenced by DMTA, may act as precursors to CEC formation, which explains the growth of Peak 2. It remains to be determined whether CECs can form from an amorphous extension alone, independent of CFC unfolding. Unfolding likely facilitates amorphous extension by reducing the constraints on amorphous chains during rearrangement. Whether the emergence of CEC also contributes to average narrowing is unclear given competing dynamics under strain along the *c*-axis: CECs may narrow if chains are pulled out, whereas lateral incorporation of uncoiled amorphous chains into the CECs can cause widening.

Some studies have found that stretching results in simultaneous narrowing and lengthening of polymer crystals.[19,41] For example, Mochizuki et al.'s study on melt-spun PCL fibers found that longitudinal crystal length along the fiber axis increased when stretched to 1:9.[19] Interestingly, that study, which uniquely identified a (0 0 14) peak, also noted that the crystal width and volume decreased upon stretching. Applying these findings to our study raises the possibility that strain-induced Peak 2 crystals may be volumetrically smaller than Peak 1 crystals, provided that the morphological stability of Peak 2 crystals is greater. Although evidence of volumetric shrinkage upon stretching would further support the notion that each subpeak corresponds to distinct crystal morphologies, we were unable to confirm this due to the absence of a peak with a nonzero *l*-index in our XRD measurements, as explained in SI 4.

Overall, our DSC and XRD findings indicate that stretching promotes the formation of crystals with greater thermodynamic stability and decreases the average crystal width. Coupled with the understanding that the unfolding of CFCs and uncoiling of amorphous chains may increase the CEC fraction, these observations suggest that the CFC is associated with Peak 1 and the CEC with Peak 2.

3.7. Crystallinity. X_c calculations derived from DSC (eq 1) and XRD data (eq 2) showed differing trends regarding the influence of stretching on X_c. Although measured X_c often differs between instruments,[10,66] relative X_c comparisons of samples measured using the same instrument remain valuable. Our DSC-derived X_c values (Figure S26) are comparable to those found in the literature,[20,22,50] but the relationship between stretching and X_c is inconsistent across these studies. Through various degrees of stretch, an insignificant difference in DSC-derived X_c was observed, averaging 50.10 ± 1.39%. However, XRD-derived X_c (Figure S27) increased with stretch, from 32.28% at 1:1 to 61.36% at 1:6, a trend generally reflected in the literature on ES fibers made from PCL and other polymers.[13−16,20,49] A potential explanation for the discrepancy

https://doi.org/10.1021/acsapm.5c00907
ACS Appl. Polym. Mater. 2025, 7, 8504−8518

between our DSC and XRD data lies in the XRD peak broadening effect of the small crystals. This would render the diffraction peaks from prepeak crystals harder to detect, thereby underestimating XRD-derived X_c at low degrees of stretch.[67] Additionally, the consistent fwhm of the tan(δ) peak through stretching suggests a constant X_c, as discussed in Section 3.4, thereby bolstering our confidence in the X_c trends observed from DSC.

4. CONCLUSIONS

In this study, ES PCL filaments were uniaxially stretched to varying degrees after electrospinning. With increasing stretching, microfibers within filaments became more aligned but also exhibited necking and coalescence resulting from the heat dissipated during plastic deformation. The initial stages of microstructural evolution involved melting of unstable crystals, amorphous chain extension, and lamellar fragmentation of the main CFC population. The extension of amorphous chains with stretching was indicated via DMTA by an increase in T_g and lower relative energy dissipation during glass transition. Fragmentation of CFCs into smaller blocks at low strains was evidenced via 1D XRD by the reduction in average crystal width, while the fraction of original crystals remained constant. At high degrees of strain beyond 1:4, DSC showed the development of a more thermodynamically stable crystal population as the fraction of the original crystal population decreased. This new population was distinct from the original crystals not just in T_m but also in its kinetic barrier to melting. High strains caused unfolding, or "melting," of CFC dominating the crystal fraction of unstretched filaments. Elongated chains, originating from CFCs and the amorphous phase, recrystallized into narrower CECs oriented along the stretch axis, as shown via 2D XRD. Our proposed mechanism for stretch-induced crystal transformation for ES PCL was supported by thermodynamic theory and literature findings on other semicrystalline polymers.

To bolster confidence in our model, future investigations may consider performing 1D and 2D XRD analyses at a greater number of intermediate stretching stages to more precisely determine how crystal dimensions and orientation evolve with strain (i.e., whether a monotonic relationship exists). Single-fiber 2D XRD scans could more directly reveal crystal alignment within individual fibers, avoiding convolution from fiber misalignment within the filaments. SAXS may be particularly valuable due to its ability to measure interlamellar distances and thereby validate our findings on amorphous extension, lamellar fragmentation, and crystal morphology.[17] Additionally, AFM can offer direct visualization of nanostructural chain-packing on fibril surfaces.[34]

Our findings reveal significant microstructural changes due to stretching, which are known to affect the material's degradative and thermomechanical properties, such as stiffness and elasticity. This has profound implications for load-bearing implants, which must provide sufficient strength to maintain structural integrity during tissue regeneration, while offering enough flexibility to prevent fibrotic responses and support knee mobility. In stretched fibers, the greater CEC fraction, coupled with improved fiber alignment, might enhance axial tensile stiffness.[68] The higher T_g of the extended amorphous chains could make stretched filaments less rubbery at physiological temperatures. Chain alignment may hinder solvent penetration and the hydrolysis of PCL's ester bonds due to greater chain compaction within the fiber,[18] potentially slowing the loss of mechanical strength. The coalesced adhesion of fibers during stretching, first reported here, may also limit degradation while unfavorably reducing porosity—necessary for nutrient migration and cell growth during tissue regeneration. Future integration of biological cues and anti-inflammatory drugs into polymeric yarns to promote regeneration may also influence crystallization and subsequent material properties.[45]

A deeper understanding of the material's microstructure is especially valuable for developing more accurate models to predict behavior under physiological conditions, such as mechanical loading, fluid exposure, and body temperature, as well as guiding the design of next-generation medical yarns. Linking structure with processing of ES filaments enables tuning of parameters, such as stretching rate and temperature, braiding speed and tension, and storage conditions during fabrication, sterilization, and packaging—all of which can influence material microstructure and, ultimately, device performance. Processing can then be tailored to optimize mechanical strength and degradation profiles for improved tissue integration with broader relevance to the development of other polymeric medical yarns. Thus, a foundational understanding of the semicrystalline architecture and its evolution during stretching paves the way for more precise engineering strategies to enhance the design of fibrous orthopedic implants.

■ ASSOCIATED CONTENT

Supporting Information

The Supporting Information is available free of charge at https://pubs.acs.org/doi/10.1021/acsapm.5c00907.

PCL chemical structure and Mw distribution; DSC curves at different sample−pan contacts, heating rates, and stretch temperatures; limitations of 1D XRD; literature values of PCL crystal sizes; lattice parameter calculation; estimation of tensile force on unit cell; OOP and IP directions on azimuthal scan; orientation factor calculation; limitations of 2D XRD; SEM micrographs and histograms presenting coalescence; expected diameter calculation; estimation of temperature increase upon stretching; SEM micrographs of fiber fraying; μCT images and corresponding coherence of filaments; theorized effect of tension on CECs and CFCs; literature mechanisms for strained deformation; studies supporting our proposed model; DMTA data of PCL T_g and epoxy softening; photographs of filament thermal contraction; simplified microstructure within fiber; and filament crystallinity measured by DSC and XRD (PDF)

■ AUTHOR INFORMATION

Corresponding Author

Hazel E. Assender − *Department of Materials, University of Oxford, Oxford OX1 3PH, U.K.*; orcid.org/0000-0001-8320-695X; Email: hazel.assender@materials.ox.ac.uk

Authors

Alana Chandler − *Department of Materials, University of Oxford, Oxford OX1 3PH, U.K.*

Ryan M. Schofield − *Department of Materials, University of Oxford, Oxford OX1 3PH, U.K.*

Pierre-Alexis Mouthuy − *Botnar Institute of Musculoskeletal Sciences, Nuffield Department of Orthopaedics, Rheumatology*

https://doi.org/10.1021/acsapm.5c00907
ACS Appl. Polym. Mater. 2025, 7, 8504−8518

and Musculoskeletal Sciences, University of Oxford, Oxford OX3 7LD, U.K.

Complete contact information is available at: https://pubs.acs.org/10.1021/acsapm.5c00907

Author Contributions

The manuscript was written through contributions of all authors. All authors have given approval to the final version of the manuscript. Conceptualization: A.C., H.E.A., P.-A.M.; methodology: A.C., H.E.A., P.-A.M.; formal analysis and investigation: A.C., H.E.A. (2D XRD: A.C., R.M.S.); writing—original draft preparation: A.C.; figures: A.C., R.M.S.; writing—review and editing: A.C., H.E.A., P.-A.M., R.M.S.; experimental resources: H.E.A., P.-A.M.; supervision: H.E.A., P.-A.M..

Notes

The authors declare no competing financial interest.

■ ACKNOWLEDGMENTS

This research was supported by the Norman Collisson Foundation and Clarendon Fund. The authors thank Richard Turner and Greg Cook for technical assistance; Dr. Colin Johnston and Nicola Flanagan of the Oxford Materials Characterization Service for training in instrumentation usage; Dr. Meng Liang for electrospinning the filament samples; Georgy Grishchenko of Prof. James Marrow's lab for obtaining the μCT scans; Drs. Andrew Lui and Gyula Zihali for XRD support; and Dr. Leonard Thomas for technical discussions. We acknowledge the use of facilities at the Henry Royce Institute at the UKAEA, supported by the EPSRC (EP/X527257/1).

■ ABBREVIATIONS

ACL, anterior cruciate ligament; AFM, atomic force microscopy; CEC, chain-extended crystals; CFC, chain-folded crystals; DMTA, dynamic mechanical thermal analysis; DSC, differential scanning calorimetry; ECM, extracellular matrix; ES, electrospun; f, Herman's orientation factor; fwhm, full width at half-maximum; G', storage modulus; G'', loss modulus; IP, in-plane; Mw, molecular weight; n, scalar multiple of original length (1:n); OOP, out-of-plane; PCL, polycaprolactone; PDO, polydioxanone; PGA, poly(glycolic acid); PLLA, poly(L-lactic acid); RT, room temperature; SAXS, small-angle X-ray scattering; SEM, scanning electron microscopy; tan(δ), damping factor; T_g, glass transition temperature; T_m, melting temperature; X_c, crystallinity; XRD, X-ray diffraction; β, azimuthal angle; θ, Bragg angle; μCT, microcomputed tomography; ∥, parallel; ⊥, perpendicular

■ REFERENCES

(1) Farajikhah, S.; Runge, A. F. J.; Boumelhem, B. B.; Rukhlenko, I. D.; Stefani, A.; Sayyar, S.; Innis, P. C.; Fraser, S. T.; Fleming, S.; Large, M. C. J. Thermally drawn biodegradable fibers with tailored topography for biomedical applications. *J. Biomed. Mater. Res., Part B* **2021**, *109*, 733−743.

(2) Abhari, R. E.; Carr, A. J.; Mouthuy, P. A.Multifilament Electrospun Scaffolds for Soft Tissue Reconstruction. In *Electrofluidodynamic Technologies (EFDTs) for Biomaterials and Medical Devices: Principles and Advances*; Woodhead Publishing, 2018; pp 295−328.

(3) Abhari, R. E.; Mouthuy, P. A.; Vernet, A.; Schneider, J. E.; Brown, C. P.; Carr, A. J. Using an industrial braiding machine to upscale the production and modulate the design of electrospun medical yarns. *Polym. Test.* **2018**, *69*, 188−198.

(4) Ferreira, T. Z.; Pan, Z.; Mouthuy, P.-A.; Brassart, L. Characterisation and modelling of continuous electrospun poly(ε-caprolactone) filaments for biological tissue repair. *J. Mech. Behav. Biomed. Mater.* **2025**, *161*, No. 106810.

(5) Wu, S.; Dong, T.; Li, Y.; Sun, M.; Qi, Y.; Liu, J.; Kuss, M. A.; Chen, S.; Duan, B. State-of-the-art review of advanced electrospun nanofiber yarn-based textiles for biomedical applications. *Appl. Mater. Today* **2022**, *27*, No. 101473.

(6) Rashid, M.; Dudhia, J.; Dakin, S. G.; Snelling, S.; Lach, A.; Godoy, R. D.; Mouthuy, P. A.; Smith, R.; Morrey, M.; Carr, A. J. Histological evaluation of cellular response to a multifilament electrospun suture for tendon repair. *PLoS One* **2020**, *15*, No. e0234982.

(7) Haghighat, F.; Abdolkarim, S.; Ravandi, H. Mechanical Properties and In Vitro Degradation of PLGA Suture Manufactured via Electrospinning. *Fibers Polym.* **2014**, *15*, 71−77, DOI: 10.1007/s12221-014-0071-9.

(8) Savić, L.; Augustyniak, E. M.; Kastensson, A.; Snelling, S.; Abhari, R. E.; Baldwin, M.; Price, A.; Jackson, W.; Carr, A.; Mouthuy, P. A. Early development of a polycaprolactone electrospun augment for anterior cruciate ligament reconstruction. *Mater. Sci. Eng., C* **2021**, *129*, No. 112414.

(9) Dias, J. R.; Sousa, A.; Augusto, A.; Bártolo, P. J.; Granja, P. L. Electrospun Polycaprolactone (PCL) Degradation: An In Vitro and In Vivo Study. *Polymers* **2022**, *14*, No. 3397.

(10) Selli, F.; Erdoğan, U. H.; Hufenus, R.; Perret, E. Mesophase in melt-spun poly(ε-caprolactone) filaments: Structure−mechanical property relationship. *Polymer* **2020**, *206*, No. 122870.

(11) Diquattro, E.; Jahnke, S.; Traina, F.; Perdisa, F.; Becker, R.; Kopf, S. ACL surgery: reasons for failure and management. *EFORT Open Rev.* **2023**, *8*, 319−330.

(12) Cheng, S. Z. D.; Jin, S.Crystallization and Melting of Metastable Crystalline Polymers. *Handbook of Thermal Analysis and Calorimetry*; Elsevier, 2002; Vol. 3, pp 167−195.

(13) Zhang, W.; Zhou, C.; Zhang, Y.; Xue, F.; Luo, B.; Li, H.; Ren, X.; Li, J.; Shang, Y.; Wu, Z.; Jiang, S. Direct investigations of temperature related structure transitions in strained poly(butylene succinate) with SAXS and WAXS. *Colloid Polym. Sci.* **2016**, *294*, 321−328.

(14) Tang, Y.; Lin, Y.; Lin, H.; Li, C.; Zhou, B.; Wang, X. Effects of room temperature stretching and annealing on the crystallization behavior and performance of polyvinylidene fluoride hollow fiber membranes. *Membranes* **2020**, *10*, No. 38.

(15) Brennan, D. A.; Shirvani, K.; Rhoads, C. D.; Lofland, S. E.; Beachley, V. Z. Electrospinning and post-drawn processing effects on the molecular organization and mechanical properties of polyacrylonitrile (PAN) nanofibers. *MRS Commun.* **2019**, *9*, 764−772.

(16) Natu, M. V.; De Sousa, H. C.; Gil, M. H. Influence of polymer processing technique on long term degradation of poly(ε-caprolactone) constructs. *Polym. Degrad. Stab.* **2013**, *98*, 44−51.

(17) Kamal, T.; Shin, T. J.; Park, S.-Y. Uniaxial Tensile Deformation of Poly(ε-caprolactone) Studied with SAXS and WAXS Techniques Using Synchrotron Radiation. *Macromolecules* **2012**, *45*, 8752−8759.

(18) Brennan, D. A.; Flamini, M. D.; Posselt, J.; Wagner, C. T.; Beachley, V. Effect of post-drawing and tension on enzymatic degradation of electrospun polycaprolactone nanofibers. *Mater. Today Commun.* **2023**, *34*, No. 104990.

(19) Mochizuki, M.; Hirano, M.; Kanmuri, Y.; Kudo, K.; Tokiwa, Y. Hydrolysis of polycaprolactone fibers by lipase: Effects of draw ratio on enzymatic degradation. *J. Appl. Polym. Sci.* **1995**, *55*, 289−296.

(20) Lim, C. T.; Tan, E. P. S.; Ng, S. Y. Effects of crystalline morphology on the tensile properties of electrospun polymer nanofibers. *Appl. Phys. Lett.* **2008**, *92*, No. 141908.

(21) Bittiger, H.; Marchessault, R. H.; Niegisch, W. D. Crystal structure of poly-ε-caprolactone. *Acta Crystallogr., Sect. B* **1970**, *26*, 1923−1927.

(22) Wang, X.; Zhao, H.; Turng, L. S.; Li, Q. Crystalline morphology of electrospun poly(ε-caprolactone) (PCL) nanofibers. *Ind. Eng. Chem. Res.* **2013**, *52*, 4939−4949.
(23) Peterlin, A.; Reinhold, C. Thermodynamic stability of polymer crystals. III. Torsional and longitudinal chain vibrations. *J. Polym. Sci., Part A: Gen. Pap.* **1965**, *3*, 2801−2810.
(24) Kobayashi, M.; Sakashita, M. Morphology dependent anomalous frequency shifts of infrared absorption bands of polymer crystals: Interpretation in terms of transition dipole-dipole coupling theory. *J. Chem. Phys.* **1992**, *96*, 748−760.
(25) Fernández-Tena, A.; Pérez-Camargo, R. A.; Coulembier, O.; Sangroniz, L.; Aranburu, N.; Guerrica-Echevarria, G.; Liu, G.; Wang, D.; Cavallo, D.; Müller, A. J. Effect of Molecular Weight on the Crystallization and Melt Memory of Poly(ε-caprolactone) (PCL). *Macromolecules* **2023**, *56*, 4602−4620.
(26) Vozniak, I.; Hosseinnezhad, R.; Morawiec, J.; Galeski, A. Microstructural Evolution of Poly(ε-Caprolactone), Its Immiscible Blend, and In Situ Generated Nanocomposites. *Polymers* **2020**, *12*, No. 2587.
(27) Wang, Z.; He, Y.; Müller, A. J. Using PCL oligomers to study the differences in melting behavior between polymers and small molecules crystals. *Polymer* **2023**, *271*, No. 125783.
(28) Lindenmeyer, P. H. Theory of polymer-chain folding. *J. Chem. Phys.* **1967**, *46*, 1902−1907.
(29) Wunderlich, B. Melting Point Variations in Linear High Polymers. *Thermochim. Acta* **1972**, *4*, 175−188.
(30) Toda, A.; Hikosaka, M.; Yamada, K. Superheating of the melting kinetics in polymer crystals: A possible nucleation mechanism. *Polymer* **2002**, *43*, 1667−1679.
(31) Ratta, V. Semicrystalline Polyimides. Virginia Tech, 1999. http://scholar.lib.vt.edu/theses/available/etd-051799-162256/.
(32) Walczak, Z. K. *Formation of Synthetic Fibers*; Gordon and Breach: New York, 1977; pp 18−30, 99−116, 123−146, 276−290.
(33) Yasuniwa, M.; Nakafuku, C.; Takemura, T. Melting and Crystallization Process of Polyethylene under High Pressure. *Polym. J.* **1973**, *4*, 526−533.
(34) Snetivy, D.; Vancso, G. J. Selective visualization of atoms in extended-chain crystals of oriented polyoxymethylene by atomic force microscopy. *Macromolecules* **1992**, *25*, 3320−3322.
(35) Bartczak, Z.; Vozniak, A. Deformation Instabilities and Lamellae Fragmentation during Deformation of Cross-linked Polyethylene. *Polymers* **2019**, *11*, No. 1954.
(36) Mouthuy, P. A.; Zargar, N.; Hakimi, O.; Lostis, E.; Carr, A. Fabrication of continuous electrospun filaments with potential for use as medical fibres. *Biofabrication* **2015**, *7*, No. 025006.
(37) Robinson, A. J.; Pérez-Nava, A.; Ali, S. C.; González-Campos, J. B.; Holloway, J. L.; Cosgriff-Hernandez, E. M. Comparative analysis of fiber alignment methods in electrospinning. *Matter* **2021**, *4*, 821−844.
(38) Kuzelova Kostakova, E.; Meszaros, L.; Maskova, G.; Blazkova, L.; Turcsan, T.; Lukas, D. Crystallinity of Electrospun and Centrifugal Spun Polycaprolactone Fibers: A Comparative Study. *J. Nanomater.* **2017**, *2017*, No. 8952390, DOI: 10.1155/2017/8952390.
(39) Schofield, R. M.; Maciejewska, B. M.; Elmestekawy, K. A.; Woolley, J. M.; Tebbutt, G. T.; Danaie, M.; Allen, C. S.; Herz, L. M.; Assender, H. E.; Grobert, N. Nanostructure and Photovoltaic Potential of Plasmonic Nanofibrous Active Layers. *Small* **2025**, *21*, No. 2409269.
(40) Wilchinsky, Z. W. On Crystal Orientation in Polycrystalline Materials. *J. Appl. Phys.* **1959**, *30*, 792.
(41) Kongkhlang, T.; Tashiro, K.; Kotaki, M.; Chirachanchai, S. Electrospinning as a new technique to control the crystal morphology and molecular orientation of polyoxymethylene nanofibers. *J. Am. Chem. Soc.* **2008**, *130*, 15460−15466.
(42) Li, W.; Zhang, D.; Qv, C.; Zhao, R.; Ma, Z. Stretching-Induced Melting and Recrystallization Polymorphism Revealed in Polybutene-1. *Macromolecules* **2023**, *56*, 2761−2771.
(43) Meyer, F.; Oldörp, K.; de Jong, F. *Dynamic Mechanical Thermal Analysis (DMTA) on Polymer Composites*; ThermoFisher Scientific, 2021; Vol. *241*, pp 1−4.
(44) Badami, D. V.; Chappel, F. P.; Culpin, M. F.; Jones, D. M.; Tranter, T. C. The effect of extension on the structure of filaments of 6.6-nylon. *Rheol. Acta* **1961**, *1*, 639−647.
(45) Zhou, Y.-H.; Yang, J.; Zhou, Z.-P.; Hao, T.-F.; Nie, Y.-J. Molecular Dynamics Simulations of Stretch-Induced Crystal Changes in Crystallized Polyethylene/Carbon Nanotubes Nanocomposites. *Chin. J. Polym. Sci.* **2023**, *41*, 1425−1438.
(46) Hill, M. J.; Barham, P. J. Ostwald ripening in polyethylene blends. *Polymer* **1995**, *36*, 3369−3375.
(47) Nam, J.; Huang, Y.; Agarwal, S.; Lannutti, J. Materials selection and residual solvent retention in biodegradable electrospun fibers. *J. Appl. Polym. Sci.* **2008**, *107*, 1547−1554, DOI: 10.1002/app.27063.
(48) Pandey, A. K.; Katiyar, V.; Takagi, H.; Shimizu, N.; Igarashi, N.; Sasaki, S.; Sakurai, S. Structural evolution in isothermal crystallization process of poly(L-lactic acid) enhanced by silk fibroin nano-disc. *Materials* **2019**, *12*, No. 1872.
(49) Wong, S. C.; Baji, A.; Leng, S. Effect of fiber diameter on tensile properties of electrospun poly(ε-caprolactone). *Polymer* **2008**, *49*, 4713−4722.
(50) Flamini, M. D.; Lima, T.; Corkum, K.; Alvarez, N. J.; Beachley, V. Annealing post-drawn polycaprolactone (PCL) nanofibers optimizes crystallinity and molecular alignment and enhances mechanical properties and drug release profiles. *Mater. Adv.* **2022**, *3*, 3303−3315.
(51) Elyashevich, G. K.; Baranov, V. G.; Frenkel, S. Y. Thermodynamics of crystallization of macromolecules of various degrees of coiling. *J. Macromol. Sci., Part B: Phys.* **1977**, *13*, 255−289.
(52) Wunderlich, B. Extended chain crystals of linear high polymers. *Pure Appl. Chem.* **1972**, *31*, 49−64.
(53) Liu, Y.; Cui, L.; Guan, F.; Gao, Y.; Hedin, N. E.; Zhu, L.; Fong, H. Crystalline Morphology and Polymorphic Phase Transitions in Electrospun Nylon 6 Nanofibers. *Macromolecules* **2007**, *40*, 6283−6290.
(54) Séguéla, R. Plasticity of semi-crystalline polymers: crystal slip versus melting-recrystallization. *e-Polymers* **2007**, *7*, No. 032, DOI: 10.1515/epoly.2007.7.1.382.
(55) Nie, Y.; Gao, H.; Hu, W. Variable trends of chain-folding in separate stages of strain-induced crystallization of bulk polymers. *Polymer* **2014**, *55*, 1267−1272.
(56) Liu, X.; Zou, L.; Chang, B.; Shi, H.; Yang, Q.; Cheng, K.; Li, T.; Schneider, K.; Heinrich, G.; Liu, C.; Shen, C. Strain dependent crystallization of isotactic polypropylene during solid-state stretching. *Polym. Test.* **2021**, *104*, No. 107404.
(57) Avella, A.; Mincheva, R.; Raquez, J. M.; Lo Re, G. Substantial effect of water on radical melt crosslinking and rheological properties of poly(ε-caprolactone). *Polymers* **2021**, *13*, No. 491.
(58) Park, J.; Eslick, J.; Ye, Q.; Misra, A.; Spencer, P. The influence of chemical structure on the properties in methacrylate-based dentin adhesives. *Dent. Mater.* **2011**, *27*, 1086−1093.
(59) Hill, D. J. T.; Perera, M. C. S.; Pomery, P. J.; Toh, H. K. Dynamic mechanical properties of networks prepared from siloxane modified divinyl benzene pre-polymers. *Polymer* **2000**, *41*, 9131−9137.
(60) Le Cam, J.-B. Energy storage due to strain-induced crystallization in natural rubber: The physical origin of the mechanical hysteresis. *Polymer* **2017**, *127*, 166−173.
(61) Toft, M. Effect of Crystalline Morphology on the Glass Transition and Enthalpic Relaxation in Poly(ether-ether-ketone). University of Birmingham, 2011. https://etheses.bham.ac.uk/id/eprint/3796/1/Toft12MRes.pdf.
(62) Sauer, B. B.; Kampert, W. G.; Neal Blanchard, E.; Threefoot, S. A.; Hsiao, B. S. Temperature modulated DSC studies of melting and recrystallization in polymers exhibiting multiple endotherms. *Polymer* **2000**, *41*, 1099−1108.
(63) Hellmuth, E.; Wunderlich, B. Superheating of Linear High-Polymer Polyethylene Crystals. *J. Appl. Phys.* **1965**, *36*, 3039−3044.

(64) Wingert, M. C.; Jiang, Z.; Chen, R.; Cai, S. Strong size-dependent stress relaxation in electrospun polymer nanofibers. *J. Appl. Phys.* **2017**, *121*, No. 015103.
(65) Youm, J. S.; Kim, J. H.; Kim, C. H.; Kim, J. C.; Kim, Y. A.; Yang, K. S. Densifying and strengthening of electrospun polyacrylonitrile-based nanofibers by uniaxial two-step stretching. *J. Appl. Polym. Sci.* **2016**, *133*, No. 43945.
(66) Doumeng, M.; Makhlouf, L.; Berthet, F.; Marsan, O.; Delbé, K.; Denape, J.; Chabert, F. A comparative study of the crystallinity of polyetheretherketone by using density, DSC, XRD, and Raman spectroscopy techniques. *Polym. Test.* **2021**, *93*, No. 106878.
(67) Sokura, L. A.; Nevedomskiy, V. N.; Baidakova, M. V.; Levin, A. A.; Belolipetsky, A. V.; Yassievich, I. N.; Ershov, A. V.; Bert, N. A. Microstructure and morphology of 2D arrays of Ge quantum dots in a Si/Al2O3 matrix. *J. Phys.: Conf. Ser.* **2020**, *1697*, No. 012135.
(68) Richard-Lacroix, M.; Pellerin, C. Orientation and Partial Disentanglement in Individual Electrospun Fibers: Diameter Dependence and Correlation with Mechanical Properties. *Macromolecules* **2015**, *48*, 4511−4519.

https://doi.org/10.1021/acsapm.5c00907
ACS Appl. Polym. Mater. 2025, 7, 8504−8518